# A Photogrammetric Approach to Fuse Natural Color and Thermal Infrared UAS Imagery in 3D Point Cloud Generation

Farid Javadnejad[1,*], Daniel T. Gillins[2], Christopher E. Parrish[1], and Richard K. Slocum[1]

***Abstract:*** The inclusion of thermal infrared (TIR) data in point clouds derived from unmanned aircraft system (UAS) imagery can benefit a variety of applications in which surface temperature and 3D geometry are both important discriminants of feature type and condition. Low resolution and narrow fields of view (FOV) of current consumer-grade TIR cameras on UAS, combined with the lack of sharpness and texture in many image regions, may cause failure or poor results from structure from motion (SfM) photogrammetric software, which has gained widespread use for generating point clouds from UAS imagery. This paper proposes a photogrammetric approach for generating 3D multispectral point clouds utilizing coacquired TIR-RGB images. A 3D point cloud is first generated from the RGB imagery using standard SfM procedures. Then the TIR attributes are assigned to points, where the image coordinates of the points in TIR images are estimated using transformation parameters obtained from co-registration procedures. To obtain RGB-to-TIR transformation parameters, this study tests 3D and 2D co-registration approaches. The latter produces better results due to the challenge of calibrating the TIR camera as required for the 3D approach. This proposed approach is advantageous for generating TIR point clouds without loss

[1] School of Civil and Construction Engineering, Oregon State University, 101 Kearney Hall, 1491 SW Campus Way, Corvallis, OR 97331, USA
[2] National Geodetic Survey, National Oceanic and Atmospheric Administration, 1315 East-West Highway, Silver Spring, MD 20910, USA
* *Corresponding author: fjnejad@lifetime.oregonstate.edu*

of photogrammetric precision compared with solely TIR-based SfM, as the 3D accuracy, point density, and reliability are greatly enhanced.

***Keywords:*** Unmanned Aircraft Systems, UAS, Thermal Infrared Imaging, TIR, Point Cloud, Fusion, Remote Sensing, Photogrammetry

## 1. Introduction

Collection and analysis of data from the thermal infrared (TIR) portion of the electromagnetic spectrum (approximately 3-15 μm) can provide unique information for identifying, describing, and monitoring objects and phenomena for a variety of remote sensing applications (Jensen 2009). Satellite TIR remote sensing utilizes advanced sensors that are very stable and radiometrically well-calibrated (Teillet et al. 2001; Roy et al. 2014), and it is used for many applications, such as meteorological studies, wildfire mapping, urban building energy efficiency, volcanology, etc. (Jensen 2009). However, the spatial resolutions available from existing satellites are coarse: for example, 1.1, 1.0 and 0.6 km from AVHRR, MODIS, and HCMM, respectively. Landsat 8 TIRS and Landsat 7 ETM+ band 6 can generate imagery resampled to a spatial resolution of 30 m (Javadnejad 2018). Such coarse resolution limits the utility of the imagery in many applications. Although airborne TIR remote sensing from conventional (manned) aircraft is possible, it is not widely available due to the high costs and time-intensive sensor calibration and processing challenges (Jensen 2009; Berni et al. 2009).

The rapid emergence of unmanned aircraft system (UAS) technology has spurred a new era in remote sensing by enabling low-cost acquisition of highly resolute spatial data with customizable revisit times (Colomina and Molina 2014; Pajares 2015; Singh and Frazier 2018; Shi et al. 2016). Aerial imaging using thermal cameras from UAS has excellent potential for close-range, high-resolution thermal remote sensing (Nishar et al. 2016). Multi-source data fusion including the TIR can supplement the information, visual content, and interpretation value of the remotely sensed data (Jixian Zhang 2010; Le Moigne, Campbell, and Cromp 2002; Brook, Vandewal, and Ben-Dor 2012). Also, processing of UAS imagery using image-based reconstruction techniques (e.g., SfM) can produce high-resolution, three-dimensional (3D) models (Wood et al. 2017; Javadnejad, Gillins, et al. 2017; Javadnejad, Simpson, et al. 2017; Slocum and Parrish 2017; O'Banion et al. 2018), which enhance the visualization as opposed to planar, 2D images from a distant satellite (Roth, Oke, and Emery 1989).

Consumer-grade thermal cameras are less expensive and have been utilized in many applications, such as building heat efficiency, electrical inspection, non-destructive testing, and leak and fire detection, etc. (Gade and Moeslund 2014; Lagüela, Díaz-Vilariño, and Roca 2016). However, there are limitations for UAS-based TIR mapping and remote sensing applications (Gade and Moeslund 2014). It is challenging to process TIR images solely using SfM, largely because the TIR images are blurred and smoothed out, due to the thermal gradient color coding that occurs in thermal focal plane arrays (FPAs) during image capture (Ham and Golparvar-Fard 2013; Sledz, Unger, and Heipke 2018). This adversely affects keypoint detection in SfM algorithms that utilize intensity gradients (Harris and Stephens 1988; Szeliski 2010). Application of mobile-lidar plus TIR sensors is not typical in UAS-based remote sensing because these systems rely on the use of global navigation satellite system (GNSS)-aided inertial navigation system (INS) (Colomina and Molina 2014), which can greatly increase cost, weight, and post-processing complexity. For separate data acquisition, the establishment of ground control points (GCPs) is challenging because GCPs must be clearly detectable in all data sources (Brook, Vandewal, and

Ben-Dor 2012; González-Aguilera et al. 2012; Lucieer et al. 2014). Moreover, the lower resolution of TIR camera will produce imagery with a coarser ground sampling distance (GSD) that reduces detail and may impact the accuracy of the 3D models (Javadnejad, Gillins, and Gillins 2016). The narrow FOV requires shorter baselines and flight lines to collect UAS imagery of the desired area with sufficient overlap, e.g., 10,000 TIR images compared to 1700 RGB images in the study by Nishar et al. (2016). Therefore, mission planning is limited by the requirements of the lower resolution TIR camera, which can significantly add to the cost of data collection and processing.

The objective of this study is to overcome some of the aformentioned challenges by introducing and evaluating an approach for fusing TIR and RGB images collected from a dual-head camera system mounted on a UAS to generate a 3D point cloud with RGB and TIR attributes. In this approach, the 3D model is first generated using only the RGB imagery. The dual-head offset between the TIR and RGB cameras implies a transformation and is used to establish a mathematical relationship for projecting points from TIR image to 3D space. This approach enables efficient generation of photogrammetrically-accurate TIR-RGB point clouds without the need for depth or INS sensors on the unmanned aircraft. This method is advantageous, because the RGB cameras have a significantly higher resolution than the thermal camera, they are commonly used in SfM software to generate 3D models. The approach also eliminates the need to establish distinct thermal GCPs.

For evaluation and as examples of implementation, coacquired TIR and RGB images from a UAS and a handheld device were processed to generate fused TIR-RGB point clouds and orthoimages. During this processing, both 3D and 2D dual-head calibration approaches were examined to co-register RGB and TIR data. In addition, for a comparison, the conventional approaches were followed to process the TIR and RGB images separately using SfM software.

The proposed approach was found to greatly enhance the 3D accuracy, point density, and reliability of the 3D TIR point clouds.

# 2. Current State-of-the-art

## 2.1. SfM Photogrammetry

SfM is a relatively new photogrammetric approach that is gaining widespread use for generation of high-resolution mapping products (e.g., point clouds and orthoimages) from overlapping imagery acquired with nonmetric, consumer-grade cameras (Javadnejad 2018). The general steps for SfM are shown in Figure 1. The process starts with automatic extraction of keypoints in the imagery. The extracted keypoints are described in descriptors (e.g., SIFT), which are matched based on the maximum likelihood of their multidimensional descriptors. A sparse point cloud is generated by simultaneously solving for the 3D location of the keypoints, as well as extrinsic orientation (EO) and intrinsic orientation (IO) parameters of the camera through bundle adjustment procedures (Lowe 2004; Snavely, Seitz, and Szeliski 2006; Snavely, Seitz, and Szeliski 2008; Triggs et al. 1999). The IO describe the optical characteristics of the camera, such as its focal length, principal point, and lens distortion coefficients, and the EO includes the 3D position and orientation of the camera (Heikkila and Silven 1997). Usually, the reconstructed model is georeferenced to a real-world coordinate system using either GCPs or via GNSS-aided INS on-board. In conventional bundle adjustment both the coordinates of the GCPs and the measured EO can be used as weighted constraints or observations. Georeferencing is typically followed by a second-step bundle adjustment to optimize the sparse point cloud, and IO and EO estimations

(Eltner et al. 2016). To complement the sparse point cloud, the multi-view stereopsis (MVS) algorithm is used to generate dense visualization comparable to lidar (Furukawa and Ponce 2010; Snavely, Seitz, and Szeliski 2008; Shao et al. 2016). Mapping products such as mesh surfaces, digital terrain models (DTMs), and orthorectified imagery is generated from sparse or dense point clouds. Some notable commercial SfM software inlcude *PhotoScan* (Agisoft 2017) and *Pix4DMapper* (Pix4D 2017), and some open source programs are *VisualSfM* (Wu 2011) and *Bundler* (Snavely, Seitz, and Szeliski 2006).

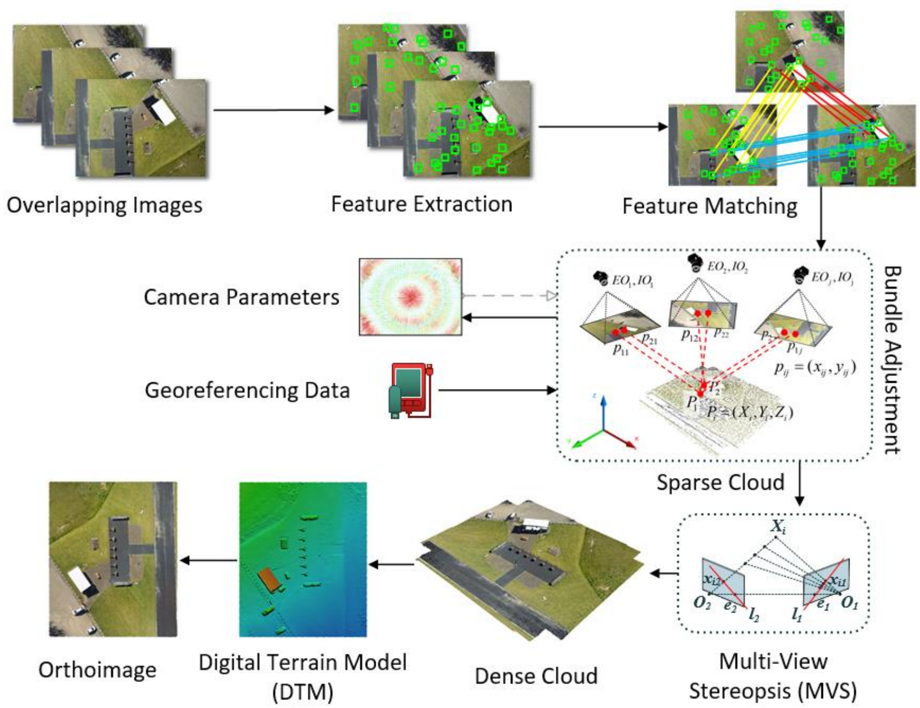


**Figure 1: SfM-MVS processing workflow (Javadnejad 2018).**

### 2.2. Multi-sensor data fusion

The integration of infrared thermography with lidar or natural color imagery is more common in building energy analysis (Kylili et al. 2014). For example, Ham and Golparvar-Fard (2013) proposed an approach for a 3D thermal reconstruction of buildings from simultaneously captured RGB and TIR using SfM, where the EO parameters of TIR camera are obtained from coacquired RGB images. The MVS densification of TIR and RGB images were processed separately to build a 3D spatio-thermal dense point cloud. Vidas et al. (2013) and Vidas et al. (2015) designed robot prototypes that utilize range sensors of Microsoft Kinect and *ASUS Xtion* to obtain depth information for integrating pre-calibrated thermal sensors (Vidas, Moghadam, and Bosse 2013; Vidas, Moghadam, and Sridharan 2015). Similarly, Borrmann et al. (2014) and Hoegner et al. (2018) presented fusion of point clouds from terrestrial lasers canners with RGB and TIR images. In a geological survey, Lewis et al. (2015) collected overlapping RGB images over a small hydrothermal unit, from which a thermal camera collected two images. A DTM was built using the RGB images, and then a thermal orthoimage was generated from orthorectification of the two thermal images. Tommaselli et al. (2010) presented an approach for registration of multi-camera setups to generate a color composite from two rectified RGB and IR images from conventional aerial photogrammetric surveys.

Multi-sensor data fusion of nonmetric UAS data is relatively new. Dios and Ollero (2006) used TIR images in combination with RGB images from a UAS to automatically detect heat loss at windows in a building based on segmentation analysis of single images. Berni et al. (2009) used photogrammetric approaches to combine UAS-based multispectral data with thermal images. The position and orientation data from the autopilot, an existing DTM, and some GCPs were used to build an orthomosaic of a corn farm. Lucieer et al., (2014) performed registration of the hyperspectral imagery and the RGB orthoimage, from separate UAS platforms, through matching GCPs within the ENVI® software (Harris Geospatial 2014). Aasen et al., (2015) developed a method for generating 3D data from hyperspectral images by processing the first band image using SfM; then, they used the alignment of the first band to create dense point clouds for all the other bands in same spatial extent. Nishar et al. (2016) deployed a UAS to collect RGB and TIR imagery with two separate flight missions over a field. RGB and TIR orthoimages were processed separately by using Pix4D Mapper, while the co-registration was done by using several aluminum GCPs visible in both datasets. Hoegner et al. (2016) collected TIR and RGB imagery with two separate flights while keeping the positions and orientations of the separate image set roughly same by using identical flight plans. Then datasets were separately processed to build 3D point clouds, and the differences between camera locations in the separate flights were corrected through a post-processing procedure. Sledz, Unger, and Heipke (2018) presented an approach to independently process RGB and TIR image to build 3D models, while using the geo-tag information from on-board GNSS to put the multi-source images in the same world coordinate system. Maset et al. (2017) presented an approach for creating 3D models directly from unordered, uncalibrated TIR images that are co-registered to an RGB point cloud though iterative closest point (ICP). Honkavaara et al. (2017) presented a technique for registration of hyperspectral bands in complex 3D scenes using tunable filters, wherein the reference bands are used to reconstruct the scene and then the bands without orientation are matched to the oriented bands.

## 3. Proposed methodology

The overarching objective of fusion is the synergistic use of multiple sensors or data streams, such that the whole is greater than the sum of the parts (Iyengar, Sastry, and Balakrishnan 2003). This work considers a specific type of fusion that involves merging data from multiple sensors to create a georeferenced data product that contains some of the best features of each. This paper proposes and tests a simplified approach for leveraging coacquired TIR-RGB images to generate thermal map products (Figure 2). The approach makes use of dual-head consumer-grade RGB and TIR cameras mounted on a moving platform, such as a UAS. In this method, only the RGB images are used to produce a traditional SfM point cloud, after which the corresponding intensity values from the coacquired TIR images are attributed to the initial 3D point. As a result, each point in the point cloud has a 3D coordinate as well as RGB and thermal attributes. This section provides a discussion of the method, including dual-head calibration, fusing of the coacquired imagery, and generation and visualization of thermal point clouds and orthoimages

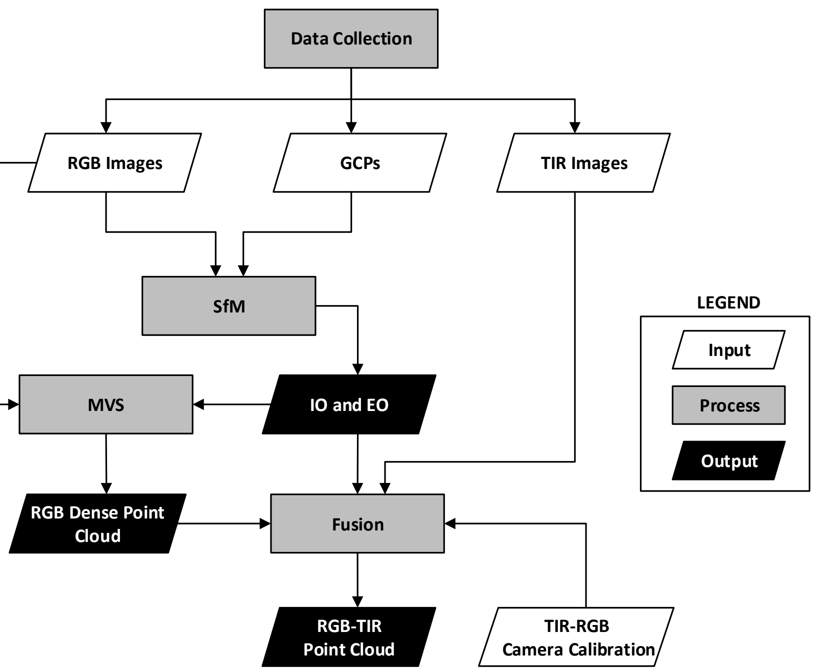


**Figure 2: Flowchart of the proposed TIR/RGB data fusion approach, presenting the inputs, outputs, and the required processing steps**

### 3.1. Fusion

Figure 3 schematically shows a dual-head camera setup mounted on a moving platform. The primary dataset $\{I\}$ is a collection of high-resolution RGB images, and the second dataset

$\{I'\}$ is a collection of low-resolution images from a thermal camera coacquired with the primary camera. The $\{I\}$ is processed using SfM to build a 3D model of the scene. The result from SfM processing is a point cloud $\{\mathbf{P}\}$ that represents the 3D geometry of the scene with RGB attributes. In mapping applications, the points are georeferenced to a geodetic datum, here called a world coordinate system (WCS), denoted as $\{{}^{W}\mathbf{P}\}$, using a conformal coordinate transformation consisting of scale, rotation and translation (${}^{w}s$, ${}^{w}\mathbf{R}$ and ${}^{w}\mathbf{T}$) (Figure 3) .

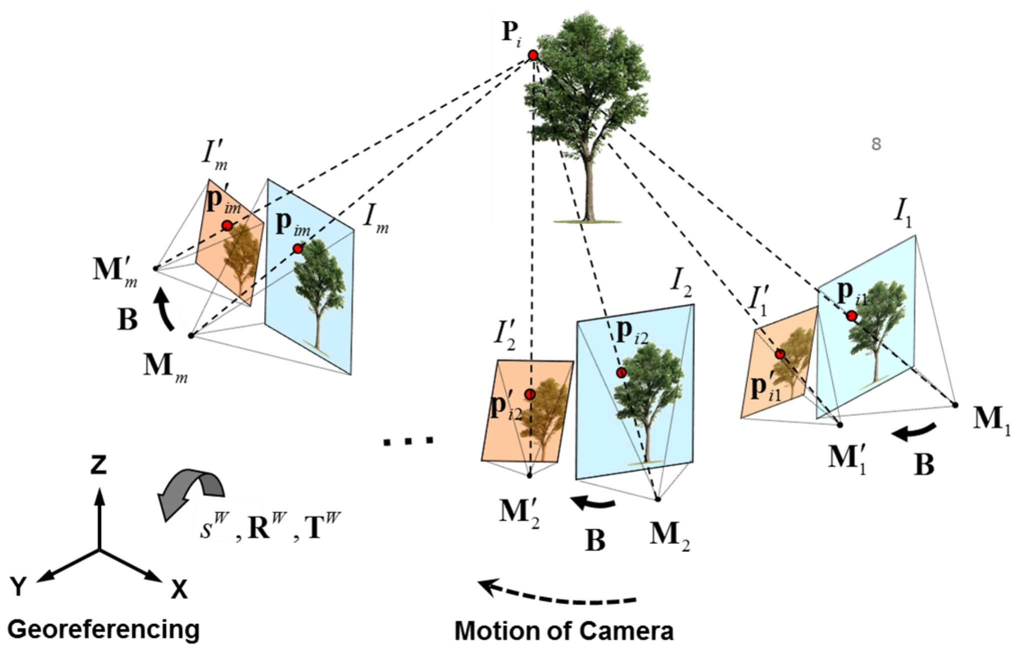


**Figure 3: A dual-head camera setup used for collecting primary and secondary images. The scene recovered using the primary image set. B represents dual-head offset between the primary and secondary cameras (Javadnejad 2018)**

Functions that map the 3D scene on 2D images in an SfM solution can be described as $\mathbf{p}_{ij} = \mathbf{M}_j \mathbf{P}_i$, where $\mathbf{p}_{ij}$ is the projection of the point $i$ on the image $j$ and $\mathbf{M}_j$ is the projection function (depending on the IO and EO for image $j$). If the transformation of extrinsics of the image $j$ ($\mathbf{R}_j$ and $\mathbf{T}_j$) are applied on the $\mathbf{P}_i$, the point coordinates in the camera coordinate system (CCS) (${}^{C}\mathbf{P}_{ij}$) is acquired (Eq. 1). The CCS is a metric 3D coordinate system with x and y-axis along the image plane and z-axis along the optical axis. The x- and y- origin is located at the image center (principal point) and negative focal length units ($-f$) out of the image plane on the z-axis. The ${}^{C}\mathbf{P}_{ij}$ can be projected on the 2D image $j$ plane using the Eq. 2 - Eq. 3 (Heikkila and Silven 1997):

$$\begin{bmatrix} {}^{C}X_{ij} \\ {}^{C}Y_{ij} \\ {}^{C}Z_{ij} \end{bmatrix} = \mathbf{R}_j \begin{bmatrix} X_i \\ Y_i \\ Z_i \end{bmatrix} + \mathbf{T}_j \tag{1}$$

$$\begin{bmatrix} x_{ij} \\ y_{ij} \end{bmatrix} = \frac{f}{{}^{C}Z_{ij}} \begin{bmatrix} {}^{C}X_{ij} \\ {}^{C}Y_{ij} \end{bmatrix} \tag{2}$$

$$\begin{bmatrix} \tilde{x}_{ij} \\ \tilde{y}_{ij} \end{bmatrix} = (1 + k_1 r_{ij}{}^2 + k_2 r_{ij}{}^4 + k_3 r_{ij}{}^6) \begin{bmatrix} x_{ij} \\ y_{ij} \end{bmatrix} + \begin{bmatrix} p_1(r_{ij}{}^2 + 2x_{ij}{}^2) + 2p_2 x_{ij} y_{ij} \\ p_2(r_{ij}{}^2 + 2y_{ij}{}^2) + 2p_1 x_{ij} y_{ij}) \end{bmatrix} \tag{3}$$

where $x_{ij}$ and $y_{ij}$ are undistorted pixel coordinates of the point $i$ in the image $j$, $f$ is the focal length, $r_{ij}{}^2 = x_{ij}{}^2 + y_{ij}{}^2$, $\tilde{x}_{ij}$ and $\tilde{y}_{ij}$ are new normalized pixel coordinate, and $k_1, k_2, k_3$ are the radial and $p_1, p_2$ are decentering lens distortion parameters of the primary camera. The pixel coordinates of the point $i$ on image $j$ (${}^{p}x_{ij}$, ${}^{p}y_{ij}$) are obtained through another coordinate system transformation to change from the 2D coordinates from the CCS into the image coordinate system of the digital image in pixels (Eq. 4) (Heikkila and Silven 1997):

$$\begin{bmatrix} {}^{p}x_{ij} \\ {}^{p}y_{ij} \\ 1 \end{bmatrix} = \begin{bmatrix} \alpha_x f & s & c_x \\ 0 & \alpha_y f & c_y \\ 0 & 0 & 1 \end{bmatrix} \begin{bmatrix} \tilde{x}_{ij} \\ \tilde{y}_{ij} \\ 1 \end{bmatrix} \tag{4}$$

where $c_x$ and $c_y$ are the principal point coordinate, and $\alpha_x$ and $\alpha_y$ are the skew coefficients. The origin of the image coordinate system is the top-left corner of image and x- and y-axes to the right and downward, respectively.

As discussed in the following 3D and 2D dual-head co-registration subsections, the proposed fusion method relates the pixel coordinates in the RGB image $({}^{p}x_{ij}, {}^{p}y_{ij})$ to the corresponding pixel in the TIR image $({}^{p+}x_{ij}, {}^{p+}y_{ij})$ using the camera models and the offset between the dual-head cameras. The mean of TIR pixel values that include $\mathbf{P}_i$ can be converted to an absolute temperature $\overline{t_i}$ using Eq. 5, where $m$ is the number of overlapping images having the point, $I'({}^{p+}x_{ij}, {}^{p+}y_{ij})$ is the image intensity value point $i$ in secondary image $j$, and $\mathrm{H}$ is a function that converts the digital number to absolute temperature values defined by radiometric calibration of the thermal camera.

$$\overline{t_i} = \mathrm{H}\left( m^{-1} \sum_{j=1}^{m} I'({}^{p+}x_{ij}, {}^{p+}y_{ij}) \right) \tag{5}$$

- *3D co-registration approach*

For a dual-head camera system, such as the setup shown in Figure 3, offset of secondary cameras with respect to the primary camera is described as lever-arm $\mathbf{T}^b$ and boresight $\mathbf{R}^b$ differences. $\mathbf{T}^b = \left[ x^b \; y^b \; z^b \right]^T$ is the distance between origin of the daul-head cameras and $\mathbf{R}^b \propto \{\omega^b, \varphi^b, \kappa^b\}$ includes sequential rotations around the x, y, and z-axis. The offset is assumed constant for a rigid-body system. Estimating the level-arm and boresight offsets requires a multi-camera calibration that is usually performed by taking multiple images of a calibration pattern, such as a checkerboard with known measurements, and solving for the IO and EO of both cameras (Heikkila and Silven 1997; Salvi, Armangué, and Batlle 2002; Bo Li et al. 2013). A specific pattern is required for TIR cameras that have different objects with variation in temperature, emissivity, and reflectivity. The EO parameters of primary and secondary images are used to estimate the lever-arm (Eq. 6) and boresight (Eq. 7) for each pair. The estimated distances and Euler angles are averaged to calculate the final offset of the dual-head camera systems.

$$\mathbf{T}^{b} = {}^{C+}\mathbf{T} - {}^{C}\mathbf{T} \tag{6}$$

$$\mathbf{R}^{b} = {}^{C}\mathbf{R}^{-1} \times {}^{C+}\mathbf{R} \tag{7}$$

Having the $\mathbf{T}^{b}$ and $\mathbf{R}^{b}$ between primary and secondary cameras, and intrinsics of secondary cameras, the equivalent pixel coordinate of the SfM points from the primary image can be estimated in the secondary image, An important distinction is that the geometry is not built using the secondary imager set because their aforementioned limitations do not allow reconstruction of the 3D point cloud through SfM procedures. However, using the proposed methodology it is possible to perform a reverse SfM and estimate the equivalent 2D coordinate in the secondary image. This approach is different than orthoretrification that involves removing the effects of image perspective and terrain to create orthoimages. Figure 4 shows the algorithm (as pseudo-code) for the 3D offset procedure. Eq. 1 is first used to calculate the coordinates of the point in the primary camera coordinate system (${}^{C}\mathbf{P}_{ij}$). Next, the coordinates of the point in secondary camera coordinate system (${}^{C+}\mathbf{P}_{ij}$) are estimated using Eq. 8. Finally, the secondary image pixel coordinates (${}^{p+}x_{ij}$, ${}^{p+}y_{ij}$) are calculated following the steps in Eq. 1 – 4, while the intrinsics of the secondary camera is used.

$$\begin{bmatrix} {}^{C+}X_{ij} \\ {}^{C+}Y_{ij} \\ {}^{C+}Z_{ij} \end{bmatrix} = \mathbf{R}^{b} \times \begin{bmatrix} {}^{C}X_{ij} \\ {}^{C}Y_{ij} \\ {}^{C}Z_{ij} \end{bmatrix} + \mathbf{T}^{b} \tag{8}$$

| | |
|---|---|
| **Inputs:** | 1. Results from SfM processing of $m$ primary images $\{I\}$<br>1.1. Georeferenced point cloud $\{{}^{W}\mathbf{P}\}$ with format ${}^{W}X, {}^{W}Y, {}^{W}Z, r, g, b$<br>1.2. Camera EO for $m$ primary images<br>2. Set of $m$ coacquired thermal images $\{I'\}$<br>3. Camera IO of secondary camera<br>4. 3D co-registration parameters (boresight rotation and lever-arm translation) |
| **Output** | Georeferenced point cloud with thermal intensity as ${}^{W}X, {}^{W}Y, {}^{W}Z, r, g, b, t$ |
| **steps** | |
| 1 | Read the $\{{}^{W}\mathbf{P}\}$ consisting of $n$ points |
| 2 | **for** $j$ =1 to m |
| 3 | Read $\{I'\}$ |
| 4 | **end for** |
| 5 | **for** $i$ = 1 to n |
| 6 | **for** $j$ = 1 to m |
| 7 | Transform ${}^{W}\mathbf{P}_i$ to ${}^{C}\mathbf{P}_i$ in CCS using Eq. 1 |
| 8 | Perform 3D co-registration transformation from ${}^{C}\mathbf{P}_i$ to ${}^{C+}\mathbf{P}_i$ using Eq. |
| 9 | Calculate coordinate of $\mathbf{p}'_{ij}$ in $I'_j$ using Eq. 2 – 4 |
| 10 | **if** point $\mathbf{p}'_{ij}$ is in $I'_j$ |
| 11 | Store the pixel value reading at $I'_j\left({}^{p+}x_{ij}, {}^{p+}y_{ij}\right)$ in a vector |
| 12 | **end if** |
| 13 | return thermal intensity vector |
| 14 | **end for** |
| 15 | Calculate the mean of thermal intensity vector using Eq. 5 |
| 16 | Convert intensity to an absolute temperature value $\bar{t}_i$ |
| 17 | Return the point ${}^{W}\mathbf{P}_i^{+} = \left[{}^{W}X_i, {}^{W}Y_i, {}^{W}Z_i, r_i, g_i, b_i, \bar{t}_i\right]^T$ |
| 18 | **end for** |
| 19 | Return the point cloud $\left\{{}^{W}\mathbf{P}^{+}\right\}$ |

**Figure 4: The algorithm for 3D co-registartion approach**

- *2D co-registration approach*

The 3D approach requires accurate calibration of both primary and secondary cameras. In consumer-grade thermal camera, in addition to the challenges of constructing a hot/cold calibration panel that differs from the traditional black and white checkerboard, it is also challenging to acquire imagery of a calibration pattern that consistently yields precise calibration results. The reason is that the uncertainty in the localization of the corners and points from a consumer-grade thermal camera, due to the lack of sharp edges between objects, is significant enough to generate mediocre results (Ellmauthaler et al. 2013; Choi, Kim, and *Ra* 2010; Hoegner et al. 2018). These limitations make the calibration of a thermal camera a challenging task (Yilmaz, Shafique, and Shah 2003). When accurate multi-camera calibration is not achievable, a 2D transformation can be used to register images in the 2D domain (Eq. 9). This simplified approach assumes that the 3D offset is small enough that perspective differences between adjacent RGB and TIR images are minimal so that the differences between the two cameras can be canceled through a 2D image-to-image affine transformation. The advantage of using affine transformation over polynomial transformations is that the latter ones use a generic model in which the coefficients do not have the same interpretability as the affine transformation and could lead to overfitting, depending on the order of the polynomial used. Additionally, since the affine transformation is just a special case of the projective transformation that preserves parallelism, so the affine transformation is sufficient and appropriate. The 2D affine transformation parameters is easily estimated through a least square adjustment of a set of corresponding feature points selected in paired images with a minimum of three pairs points (Ghilani 2011). The 2D affine transformation can be represented with four separate transformations including translation, scale, shear, and rotation as shown in Eq. 10.

$$\begin{bmatrix} {}^{p+}x_{ij} \\ {}^{p+}y_{ij} \\ 1 \end{bmatrix} = \mathbf{A}_T \times \begin{bmatrix} {}^{p}x_{ij} \\ {}^{p}y_{ij} \\ 1 \end{bmatrix} \tag{9}$$

$$\mathbf{A}_T = \mathbf{A}_t \times \mathbf{A}_s \times \mathbf{A}_\sigma \times \mathbf{A}_\theta = \begin{bmatrix} 1 & 0 & t_x \\ 0 & 1 & t_y \\ 0 & 0 & 1 \end{bmatrix} \begin{bmatrix} s_x & 0 & 0 \\ 0 & s_x & 0 \\ 0 & 0 & 1 \end{bmatrix} \begin{bmatrix} 1 & \sigma & 0 \\ \sigma & 1 & 0 \\ 0 & 0 & 1 \end{bmatrix} \begin{bmatrix} \cos(\theta) & \sin(\theta) & 0 \\ -\sin(\theta) & \cos(\theta) & 0 \\ 0 & 0 & 1 \end{bmatrix} \tag{10}$$

The 2D co-registration is a simplified approach, that compared to the 3D boresight and lever-arm calibration, it handles all but a portion of 3D differences and intrinsics of the secondary camera and including: (1) $f'$ and $z^b$ through $\mathbf{A}_s$; (2) $x^b, y^b, c'_x, c'_y$ through $\mathbf{A}_t$; (3) skew coefficient through $\mathbf{A}_\sigma$; and (4) $\kappa^b$ through $\mathbf{A}_\theta$ transformation, while $\omega^b$, $\varphi^b$ and lens distortion parameters are not considered compared to the 3D approach. For achieving better results, it recommended to first undistort the TIR images if a camera model exists. If the dual-head cameras are tilted, e.g., cameras with converging z-axis, the 2D perspective projection (Mikhail, Bethel, and McGlone 2001) will be a better choice than the affine transformation. Figure 5 shows the descriptive algorithm of the 2D image registration procedure. The main difference here is that instead of performing the 3D transformation from ${}^{C}\mathbf{P}_{ij}$ to ${}^{C+}\mathbf{P}_{ij}$ and calculating $({}^{p+}x_{ij}, {}^{p+}y_{ij})$, the $({}^{p}x_{ij}, {}^{p}y_{ij})$ is calculated first using the accurately estimated primary camera IOs. Then, the co-registration parameters are used to correct for $({}^{p}x_{ij}, {}^{p}y_{ij})$ to $({}^{p+}x_{ij}, {}^{p+}y_{ij})$ misalignment.

| | |
|---|---|
| **Inputs:** | 1. Results from SfM processing of $m$ primary images $\{I\}$<br>1.1. Georeferenced point cloud $\{{}^{W}\mathbf{P}\}$ with format ${}^{W}X, {}^{W}Y, {}^{W}Z, r, g, b$<br>1.2. Camera IO of primary camera<br>1.3. Camera EO for $m$ primary images<br>2. Set of $m$ coacquired thermal images $\{I'\}$<br>3. 2D co-registration parameters |
| **Output** | Georeferenced point cloud with thermal intensity as ${}^{W}X, {}^{W}Y, {}^{W}Z, r, g, b, t$ |
| **steps** | |
| 1 | Read the $\{{}^{W}\mathbf{P}\}$ consisting of $n$ points |
| 2 | **for** $j$ =1 to m |
| 3 |     Read $\{I'\}$ |
| 4 | **end for** |
| 5 | **for** $i$ = 1 to n |
| 6 |     **for** $j$ = 1 to m |
| 7 |         Transform ${}^{W}\mathbf{P}_i$ from WCS to $\mathbf{P}_i$ in BCS using coordinate transformation |
| 8 |         Calculate pixel coordinates of point $\mathbf{P}_i$ in image $I_j$ using Eq. 1 - 4 |
| 9 |         **if** point $\mathbf{p}_{ij}$ is in $I_j$ |
| 10 |             Calculate coordinate of $\mathbf{p}'_{ij}$ in $I'_j$ using Eq. 9 |
| 11 |             Store the pixel value reading at $I'_j\left({}^{p+}x_{ij}, {}^{p+}y_{ij}\right)$ in a vector |
| 12 |         **end if** |
| 13 |         return thermal intensity vector |
| 14 |     **end for** |
| 15 |     Calculate the mean of thermal intensity vector using Eq. 5 |
| 16 |     Convert intensity to the absolute temperature value $\bar{t}_i$ |
| 17 |     Return the point ${}^{W}\mathbf{P}_i^{+} = \left[{}^{W}X_i, {}^{W}Y_i, {}^{W}Z_i, r_i, g_i, b_i, \bar{t}_i\right]^T$ |
| 18 | **end for** |
| 19 | Return the point cloud $\{{}^{W}\mathbf{P}^{+}\}$ |

**Figure 5: The algorithm for 2D image registration approach**

## 3.2. Visualization

- *Point cloud*

Here, we propose an integrated visualization method that blends RGB colors and TIR color-map into a new color-space which accentuates relatively hot and cold regions of the point cloud. Modified from Vidas et al. (2013), the RGB values are first converted to a grayscale value ($\mathbf{C}_{Grayscale}$) generating a grayscale point cloud; then points are colored based on their temperatures ($t$) relative to the mean temperature of the point cloud ($t_{mean}$). The integrated visualization is presented in Figure 6, and is formalized in Eq. 11 and Eq. 12, where a weight ($w$) is estimated in order to assign a higher color intensity for temperature color-map ($\mathbf{C}_{Colormap}$) at hot and cold regions versus the grayscale point cloud. The mapper can assign an $L$ value between 0 and 1 in order to control the relative brightness of the grayscale point cloud. For example, if the scene includes items with bright objects, the user can change $L$ to decrease the brightness and enhance visualization of temperature.

$$\mathbf{C}_{Fused} = w \times \mathbf{C}_{Colormap} + L \times (1-w)\left(\mathbf{C}_{Grayscale}\right) \tag{11}$$

$$w = \begin{cases} \dfrac{t - t_{mean}}{t_{\max} - t_{mean}}, & t > t_{mean} \\ \\ \dfrac{t_{mean} - t}{t_{mean} - t_{\min}}, & t < t_{mean} \end{cases} \tag{12}$$

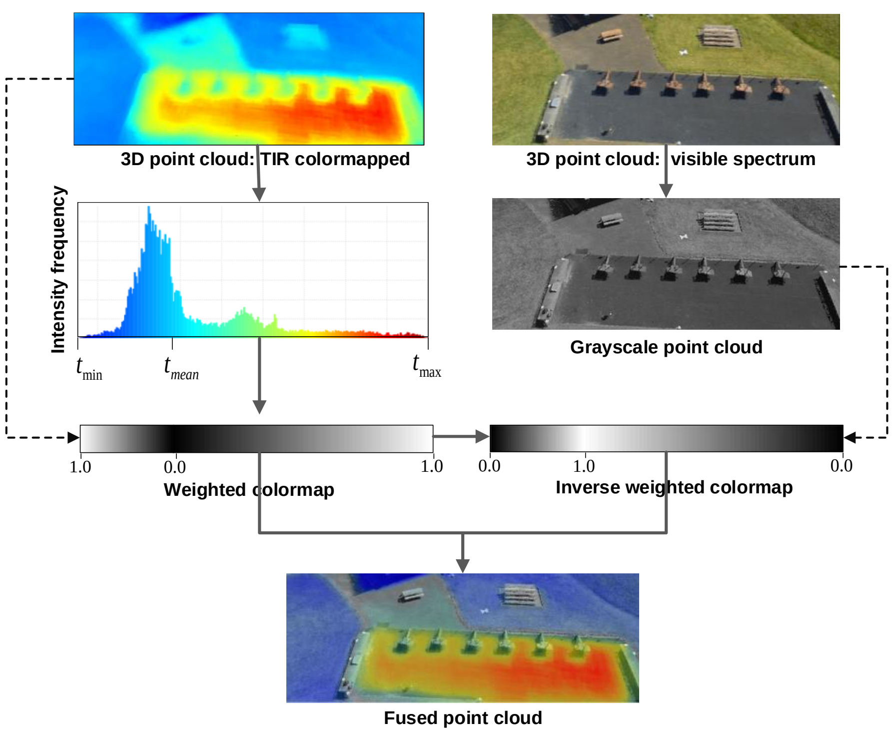


**Figure 6: The proposed approach for integrated visualization of 3D RGB-TIR point clouds**

- *Raster*

It is possible to generate planimetric mapping products from a 3D model, such as a DTM and an orthoimage. A TIR orthoimage can be generated from the point cloud by interpolating the point cloud onto a regular x-y grid and assigning thermal intensity as the z-values. The most common interpolating techniques include natural neighbor, inverse distance weighted (IDW), triangulated irregular network (TIN), and kriging (Guo et al. 2010; Javadnejad 2013; Javadnejad, Waldron, and Hill 2017). The proposed method of integrating RGB-TIR-DTM data is through building a hillshade raster of the DTM and integrating it with grayscale color composed of RGB data (Nagi 2012; Javadnejad, Alinia, and Behnia 2011), then overlaying the composite grayscale image with a transparent color-mapped TIR image. The implementation of this approach is later presented in the results section.

## 4. Experimental datasets and data processing

The proposed approach was tested on images taken by two systems with dual-head TIR and RGB cameras. A checkerboard with thermal and visible calibration patterns was used to perform boresight and lever-arm calibration for camera sets. First, the RGB and TIR images were processed separately using *PhotoScan* 1.3 (Agisoft 2017) to generate conventional SfM point clouds. Georeferencing was performed by identifying the GCPs in the images and providing the known coordinates as presented by Javadnejad and Gillins (2016). A mask was applied to TIR images to omit pixels overwritten with header pixels, logos or scale bars. In the case that SfM-MVS from the TIR images was feasible, the accuracy of reconstruction is evaluated. The proposed 2D and 3D co-registration approaches are used to generate fused RGB-TIR point clouds. The performance of the RGB-TIR co-registration through the proposed techniques is evaluated by making 3D distance measurements on point clouds between a number of features distinguishable in the RGB and TIR images.

### 4.1. Platforms

The platforms for testing include a FLIR® E6 handheld unit (Figure 7a) and a senseFly® albris UAS (Figure 7b). Both platforms are equipped with dual-head TIR-RGB cameras with specifications listed in Table 1. The FLIR E6 has a comparatively better thermal camera (160 × 120 pixels), and the albris has a higher resolution RGB camera (38-megapixel), but a very low-resolution TIR camera (80 × 60 pixels). Ideally, the dual-head cameras should be perfectly synchronized; however, in practice, the synchronization will have some error due to difference in frame rates and triggering systems responses. Due to the extended processing and storing time of the higher-resolution RGB images, the time synchronization error is more substantial in the albris than for the E6.

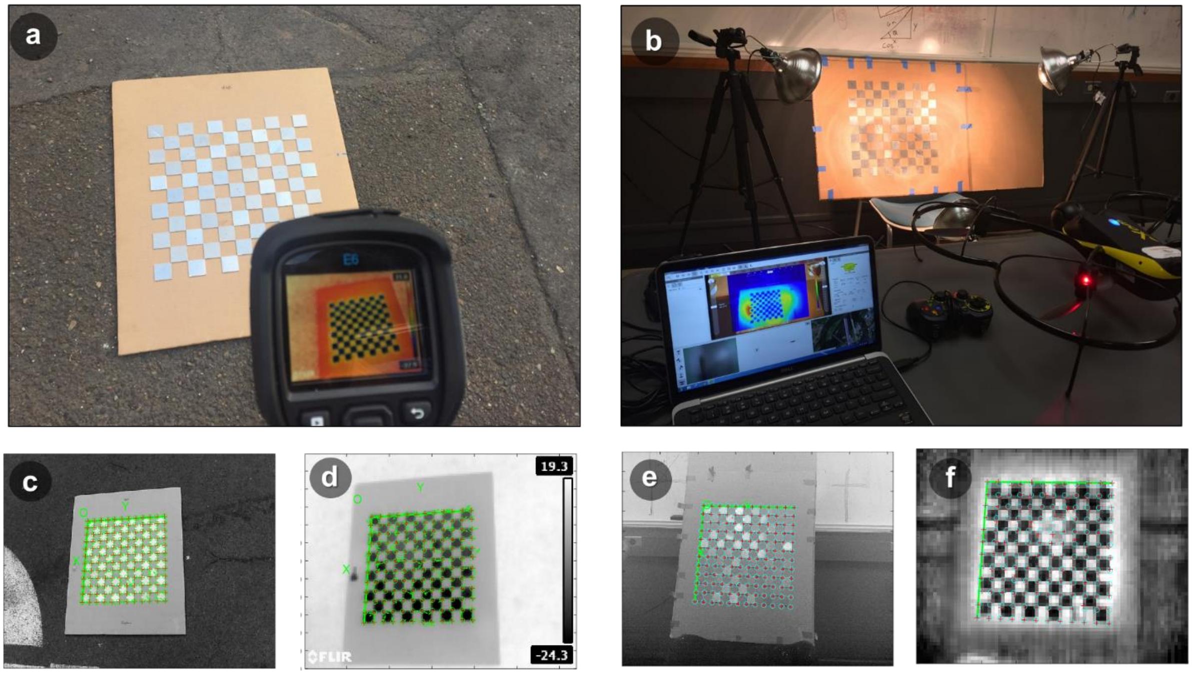


**Figure 7: (a) The FLIR E6 handheld thermal camera and the calibration tool with high reflectivity pattern, (b) senseFly albris UAS platform and its ground station displaying first-person view (FPV) thermal video stream from a heated thermal calibration tool, (c) and (d) example of coacquired visible-TIR images taken by FLIR E6 of a calibration pattern and the extracted corners, and (e) and (f) example of coacquired RGB-TIR images taken by senseFly albris of a calibration pattern and the extracted corners**

For both platforms, the image intensity values were converted to absolute temperature values (Eq. 5) using the factory radiometric calibration information. The albris stores the temperature data in units of milliKelvin (mK) in raw image format. However, the E6 does not support the raw output, but stores the processed, color-mapped TIR images in jpeg format. To convert the E6 values, data collection was operated with a fixed temperature range with $T_{\min}$ and $T_{\max}$ as the minimum and maximum temperature values. Using the fixed bar temperature range the intensity reading on image ($i$) was converted to gray-scale and then to temperature values using Eq. 13:

$$T = \frac{\left(i - i_{\min}\right)\times\left(T_{\max} - T_{\min}\right)}{\left(i_{\max} - i_{\min}\right)} + T_{\min} \tag{13}$$

where $i_{\min}$ and $i_{\max}$ range between 0 and 255, and are the minimum and maximum intensity value readings in the gray-scale image.

**Table 1: Description of platforms used for collecting the experimental data (FLIR 2018; senseFly 2017)**

| Attribute | Platform | |
|---|---|---|
| | **senseFly albris (eXom)** | **FLIR E6** |
| RGB Camera | Nokia Lumia | FLIR E6 |
| Resolution | 7152 × 5368 pixels | 640 × 480 pixels |
| FOV | 63° × 47° | 55° × 43° |
| File format | RAW | Jpeg |
| TIR Camera | FLIR One | FLIR E6 |
| Detector type | Uncooled microbolometer | Uncooled microbolometer |
| Resolution | 80 × 60 pixels | 160 × 120 pixels (resampled to 320 × 240) |
| FOV | 50° × 38° | 45° × 34° |
| Sensitivity | 150 mK | 60 mK |
| Accuracy | ±3 °C or ± 5% of reading | ± 2 °C or ± 3% of reading |
| Spectral range | 8 – 14 µm | 7.5 – 13 µm |
| Frame rate | 9 fps | 9 fps |
| File format | RAW | jpeg |
| Platform Type | UAS | Hand-held |

### 4.2. Camera calibration

An 11 × 11 checkerboard pattern made of cardboard paper and highly reflective metal squares of 1.5 inches (38.1 mm) was used to create a thermal calibration pattern. The thermal contrast was generated for calibrating the handheld E6 camera by holding the calibration pattern to reflect the cold sky (Figure 7d). The thermal contrast was generated for calibrating the albris by using heat lamps (Figure 7f). In total, 80 RGB-TIR image pairs of the checkerboard were collected using each platform. The calibration was performed using the Caltech Camera

Calibration Toolbox for *MATLAB*® (Bouguet 2004) to estimate the IO and EO of RGB and TIR cameras. Figure 7c – 7f show examples of pairs of images taken by the cameras, where the corners were extracted for calibration of the cameras. The boresight and lever-arm differences were calculated using the Eq. 6 and 7. The 2D affine transformation parameters for image registration were estimated by using the matching points in the paired images. The 2D coordinates of the extracted points from the toolbox (i.e., 144 per each image) were used to calculate the parameters of the affine transformation.

The boresight and lever-arm calibration was found to be a challenging task due to the very low-resolution TIR images which are often blurry. As presented in Table 2, the coefficient of variation (COV) of the estimates are substantial, and this problem can also be caused by weak configuration of a number of image pairs. This highlights the previous discussion on the difficulty of obtaining accurate multi-camera calibration parameters for TIR images and explains why the 2D co-registration parameters ultimately yields better estimates compared to the 3D approach. This shortcoming also underscores some of the difficulty of working with consumer-grade, low-resolution TIR cameras; nevertheless, the research presented herein aims to study the usability of such cameras which are often used in UAS remote sensing.

**Table 2: Summary of boresighting and image registration parameters.**

| Registration Technique | Parameter | FLIR E6 | | | senseFly albris | | |
|---|---|---|---|---|---|---|---|
| | | Estimated | St. Dev. | COV | Estimated | St. Dev. | COV |
| 3D boresighting | $\omega^b$ (deg) | 0.1015 | 0.2594 | 255% | 0.6950 | 1.5462 | 222% |
| | $\varphi^b$ (deg) | 0.0700 | 0.5726 | 818% | -1.5534 | 5.0437 | 325% |
| | $\kappa^b$ (deg) | 0.0670 | 0.6422 | 958% | -0.0882 | 5.4451 | 6170% |
| | $x^b$ (mm) | -0.8 | 2.5 | 313% | 16.2 | 13.9 | 86% |
| | $y^b$ (mm) | -15.0 | 2.4 | 16% | 38.4 | 9.1 | 24% |
| | $z^b$ (mm) | 28.8 | 8.4 | 29% | 45.5 | 35.7 | 78% |
| 2D image registration | $t_x$ (pix) | 77.9 | 1.9 | 2% | 743.1 | 140.2 | 19% |
| | $t_y$ (pix) | 41.9 | 3.3 | 8% | 704.8 | 108.6 | 15% |
| | $\theta$ (deg) | 0.3683 | 0.4269 | 116% | 0.6891 | 1.8950 | 275% |
| | Scale | 1.535 | 0.008 | 1% | 66.691 | 2.468 | 4% |
| | Shear | 0.005 | 0.010 | 211% | 0.009 | 0.050 | 549% |

### 4.3. Sites

The locations of the sites are shown in Figure 8, and the summary information of the datasets is listed in Table 3. The pair images were collected following different patterns and orientations for each site, e.g., unorganized, oblique for site 1, circular for site 2, and nadir, aerial for site 3.

- *Site I: Kearney Hall*

This site is the exterior of Kearney Hall on Oregon State University Campus in Corvallis, Oregon (Figure 8b). The handheld E6 was used to collect 95 terrestrial RGB-TIR image sets, such as those shown in Figure 8c. The data was collected after sunset with an average ambient temperature of 18°C (Table 3). The models were georeferenced by placing markers on a number of window corners. The 3D coordinates of the corners were obtained from matching window corners in an existing lidar dataset (Figure 9a) that was collected in 2015 (Mahmoudabadi, Olsen, and Todorovic 2016). The same lidar dataset was also used to estimate the accuracy of the 3D reconstruction by performing a cloud-to-cloud comparison (Lague, Brodu, and Leroux 2013) between the lidar and SfM-MVS point cloud in Cloud Compare (Girardeau-Montaut 2017). The section of the lidar point cloud including Kearney Hall had 4.6 million points, as listed in Table 3.

- *Site II: Brownsville power station*

This site is a power substation managed by Pacific Power (https://www.pacificpower.net) located in Brownsville, Oregon (Figure 8b). The albris was deployed to collect RGB-TIR (example imagery is shown in Figure 8c). For safety purposes, the flights were carried out with 20 feet clearance from all electrical equipment, 20 feet clearance from the facility fence, and without directly flying over the equipment. To minimize the impact of the uncertainty in the time-synchronization between the RGB and TIR imagery acquired from the albris, the flights were conducted on a day with no wind and a low flight speed (Table 3). In total, 165 images were collected during three automated flight missions with horizontal and cylindrical patterns. The flight pattern (image alignments) is shown in Figure 8d. For georeferencing, 17 GCPs were placed on the site and were surveyed using a dual frequency GNSS rover in real-time kinematic mode utilizing the Oregon Real-time GNSS Network (Allahyari et al. 2018; Tahami et al. 2018).

- *Site III: Adair RC club*

This site is the Brian Unwin Field, Benton County Radio Control (RC) Club's field in Adair Village, Oregon (Figure 8b). The field has sufficient thermal contrast with a black material RC airplane runway, a small wooden cabin building, and grass. The UAS platform, the GCP network distribution, and the surveying technique for establishing GCPs were similar to site II. Two flights were conducted at 100 and 45 m above ground level (AGL). The first flight aimed at collecting imagery of the overall site, and the second collected detailed imagery of the building. Both flights were operated in a nadir, aerial photogrammetric pattern with 90% sidelap and endlap, resulting in the collection of 101 images (Table 3).

**Table 3: Summary of sites and the platforms used for data collection**

| Attribute | Site 1 | Site 2 | Site 3 |
|---|---|---|---|
| # of images | 95 | 165 | 101 |
| Platform | FLIR E6 | SenseFly Albris | SenseFly Albris |
| Size of site | 60 m × 60 m | 50 m × 70 m | 140 m × 170 m |
| # of GCPs | 7 | 14 | 11 |
| RMSE georeference | 3.9 cm | 1.8 cm | 2.6 cm |
| # of points | 975 k | 19 M | 8 M |
| Ambient Temperature | 18 °C (sunset) | 7 °C (cloudy) | 28 °C (sunny) |
| Date | July 11, 2017 | November 19, 2016 | May 3, 2017 |
| Description | Kearney | Brownsville | Adair |

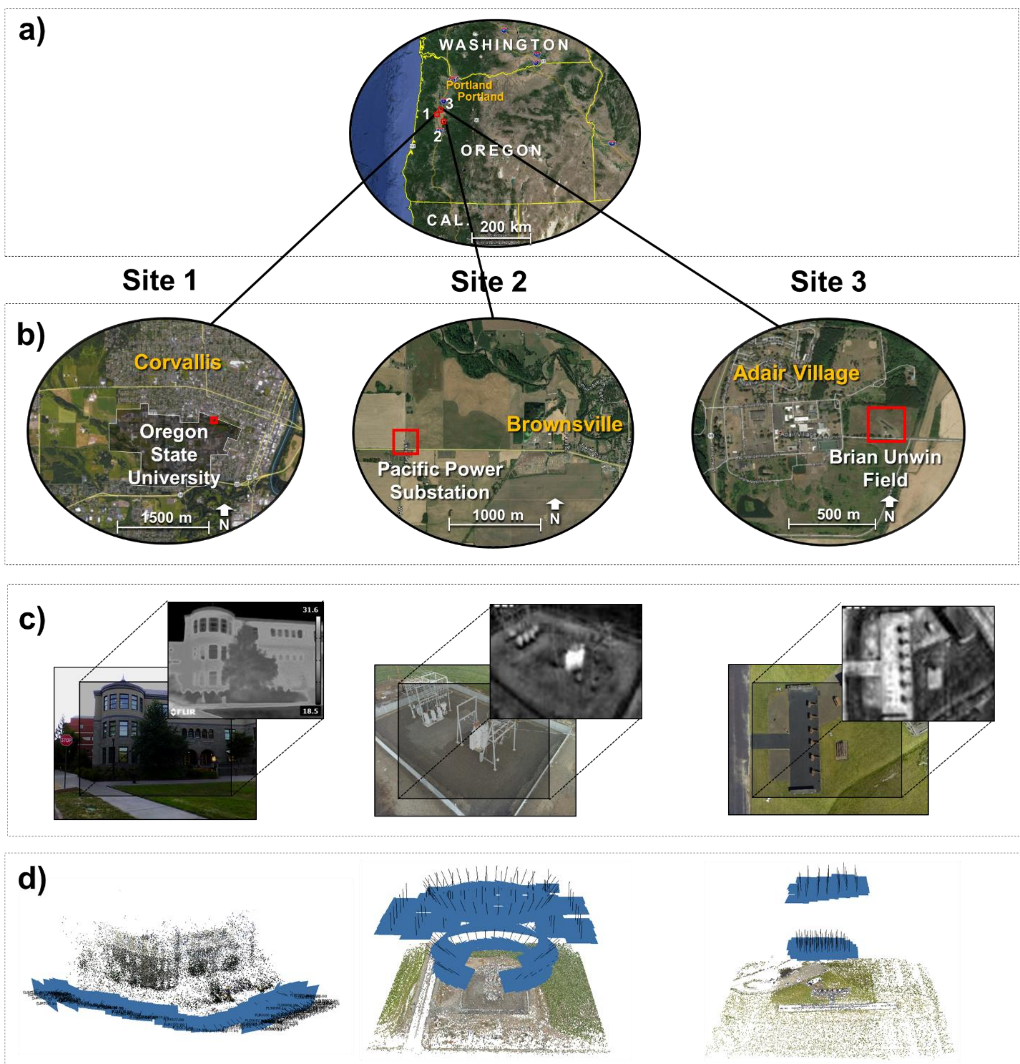


**Figure 8: The case study dataset. (a) overview map, (b) location of sites, (c) examples of coacquired RGB and TIR images, and (d) RGB sparse point clouds resulted from post-processing of the images in *PhotoScan*, where the blue panels represent the location and orientation of the RGB images in data collection.**

### 4.4. Data processing

The location and orientation of the cameras for RGB images of the sites resulted from *PhotoScan* is presented in Figure 8d; in addition, the dense RGB point clouds for sites 1, 2 and 3 are presented in Figure 9b, 10a, and 11a, respectively. Direct SfM processing of only the TIR images was challenging and hardly successful for the three sites. For instance, the SfM processing of only the TIR images for site 1 resulted in a 3D point cloud that was not geometrically rich with low point density (Figure 9c), as there were only 103,175 points in the TIR point cloud compared to 970,959 points in the RGB point cloud (Table 3).

A cloud-to-cloud comparison between the TIR or RGB point clouds for site 1 with the existing lidar data also showed a considerable relative difference. The root-mean-square of the 3D error ($RMSE_{3D}$) was calculated in *CloudCompare* based on absolute 3D distances ($L_{C2C}$) (Lague, Brodu, and Leroux 2013) between the SfM-MVS and lidar point clouds. The $RMSE_{3D}$ was 0.23 m for the RGB model (Figure 9b) and 1.96 m for the TIR model (Figure 9c) of in site 1. Unfortunately, SfM processing of the TIR images for sites 2 and 3 failed to reconstruct the 3D geometries.

The proposed methodologies for 3D and 2D co-registration were developed using custom *MATLAB*® scripts based on the algorithms described in Figure 4 and Figure 5. The dense RGB point clouds from *PhotoScan* were stored as ASCII text files, and the estimated camera IO and EO parameters were exported as Extensible Markup Language (XML) files. The *MATLAB* scripts read the output from *PhotoScan*, including the initial RGB point cloud (ASCII file) and the camera parameters (XML file) to estimate the image coordinate of the points in TIR images. Then the thermal intensity values are mapped on the point cloud as an additional TIR field. In addition, custom *MATLAB* tools were developed to generate fused visualization with integrated RGB-TIR color-mapped point clouds based on Figure 6. In order to quantify the registration error in the proposed approaches, the root-mean-square error of registration, $RMSE_{Reg}$, was calculated by making 3D distances measurements between distinct features that are detectable in both the RGB and TIR point clouds. The measurements were made in the RGB-TIR fused visualization using *CloudCompare* for about 20-25 points.

The TIR orthoimage was generated from 2D image registration TIR point cloud using the cloud to raster conversion tool in *CloudCompare*. *PhotoScan* and *CloudCompare* are able to generate the RGB orthoimage and DTM raster files; nevertheless here the result from *CloudComapre* is utilized. In order to integrate all RGB-TIR-DTM data into a single raster for better visualization, the resultant raster data were imported into *Esri®* *ArcMap* (Esri 2016). As described in the proposed methodology section, a hillshade model was generated from the DTM in ArcMap; then the RGB orthoimage was converted to a grayscale image, which was later integrated with a hillshade model in *ArcMap*. The resultant combined raster (featuring color and topography), was overlaid by the transparent layer of the color-mapped TIR orthoimage.

## 5. Results and Discussion

Figure 9d and Figure 9e show the TIR point cloud for site 1 using the proposed 3D and 2D co-registration approaches, respectively. A brightness value of $L$ = 0.8 (Eq. 11) was used for a better presentation of the bright objects in the grayscale point cloud. Similarly, the results for site 2 and 3 are shown in Figure 10 and 11. Both 3D and 2D co-registration approaches were able to construct 3D TIR point clouds; however, the results of the 3D approach method were not stable for all three sites. The $RMSE_{Reg}$ is considerably higher for the 3D approach: 1.27 m and 4.85 m for sites 1 and 3, as compared with 0.22 m and 0.20 m for the same sites using the 2D approach (Figure 9e, 11c). The relatively poorer result from the 3D approach is believed to be due to the inaccurate/imprecise camera calibrations and the subsequent multi-camera boresight differences estimates. This issue can be seen in Table 2, where estimated boresight parameters, especially the rotations values, have a considerably high COV. In contrast, the use of the same extracted checkerboard corners for estimating the 2D approach yields smaller variation and more precise results, showing that the platform with a higher resolution TIR camera was able to yield a calibration model with improved accuracy.

Figures 9f, 10d and 11d show the TIR-RGB fused, color-mapped point clouds for the experimental datasets. In addition, Figure 12d shows a fused, color-mapped orthoimage of site 3 that is made of the grayscale RGB orthoimage (Figure 12b) integrated with the hillshade model (Figure 12c), which finally was overlaid with a 20-percent transparent, color-mapped TIR orthoimage (Figure 12a).

The inclusion of both RGB and TIR data in the 3D point cloud significantly enhances visual analysis of the final product, as can be seen in Figures 9f, 10e and 11d. The fusion method allows visualization of the thermal data while inheriting the higher accuracy and resolution of the RGB point cloud.  In addition, since the data are referenced together, maps can also be made by overlaying a TIR orthoimage from the point cloud on the RGB orthoimage, as depicted in Figure 12d.  Following the proposed approach, all map products can be scaled to the real world without a need for thermal GCPs that can be difficult to establish in the survey. For example, site 1 uses a local coordinate system, while sites 2 and 3 utilize NAD 83(2011) Epoch 2010.0 Oregon State Plane North (FIPS 3601) coordinates. Having data in a known coordinate system significantly enhances its utility, by enabling overlay with other georeferenced data products and subsequent geospatial analysis in a GIS.

Besides possible shortcoming of the registration techniques, inaccurate thermal readings and thermal drift can cause overlapping TIR images to have different thermal values at the same location. The reported thermal accuracy for the TIR cameras tested in this study is about ± 3 °C or ± 5% of the readings. Thermal drift might also result in a change in the temperature of the environment from one flight to other flight, especially for larger sites or from flights at different times of the day. Computing and using the mean or median of the thermal values from several overlapping images of a point (Eq. 1) appears to reduce the effects of drift. The redundant observations help to generate a seamless thermal model in areas with several overlapping images. In locations with limited or minimal image overlap, thermal drift may create a pseudo-thermal gradient, such as can be seen near the edges of Figure 12d.

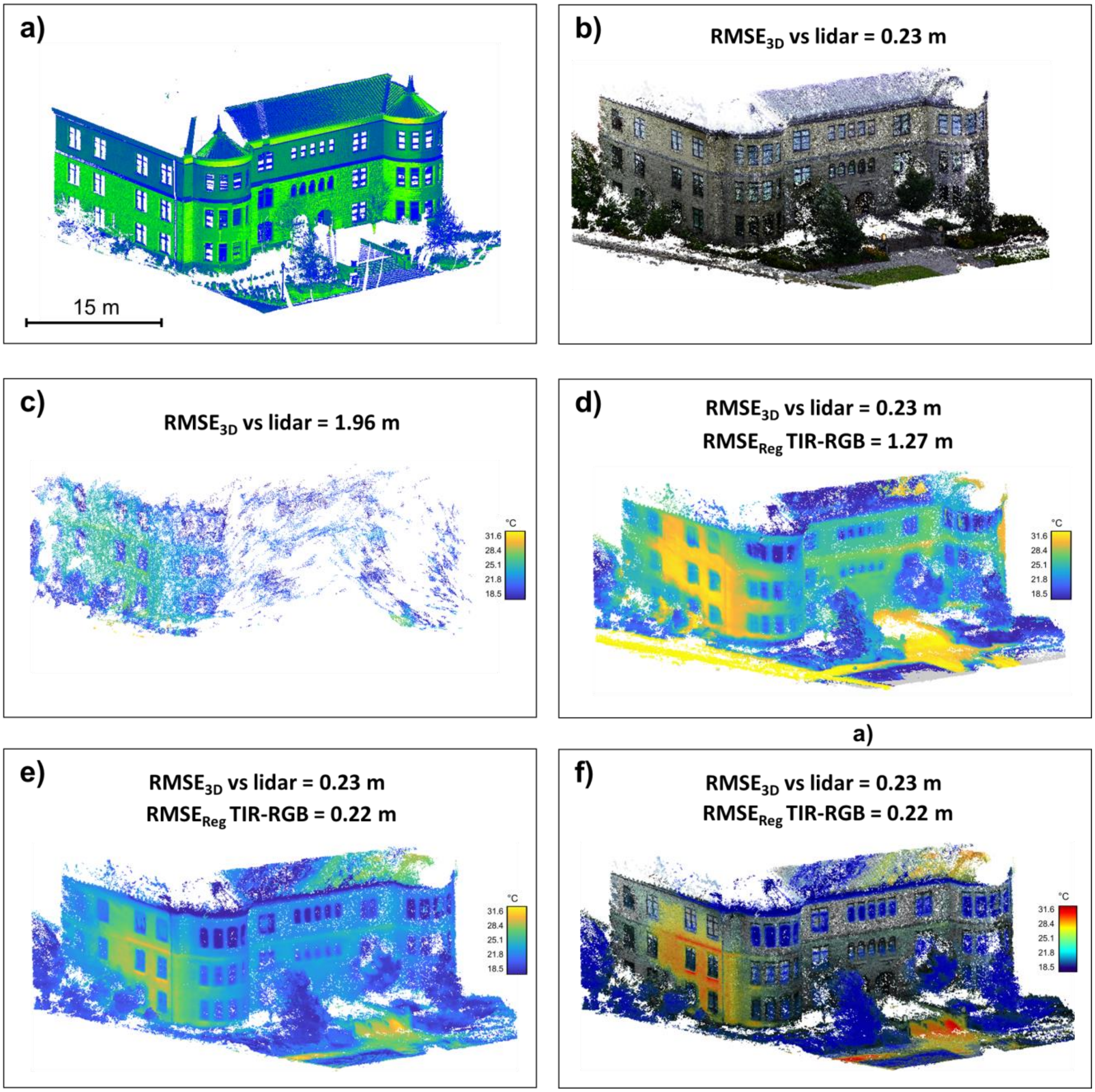


**Figure 9: (a) the lidar point cloud for Kearney Hall (site 1); this lidar point cloud was used for georeferencing SfM models and accuracy assessment of SfM-MVS models; (b) dense RGB point cloud resulted from SfM-MVS, (c) 3D point cloud directly processed from TIR images (d) TIR 3D point clouds resulted from 3D boresighting approach, (e) TIR 3D point cloud resulted from 2D image registration approach (f) fused RGB-TIR 3D point cloud visualization**

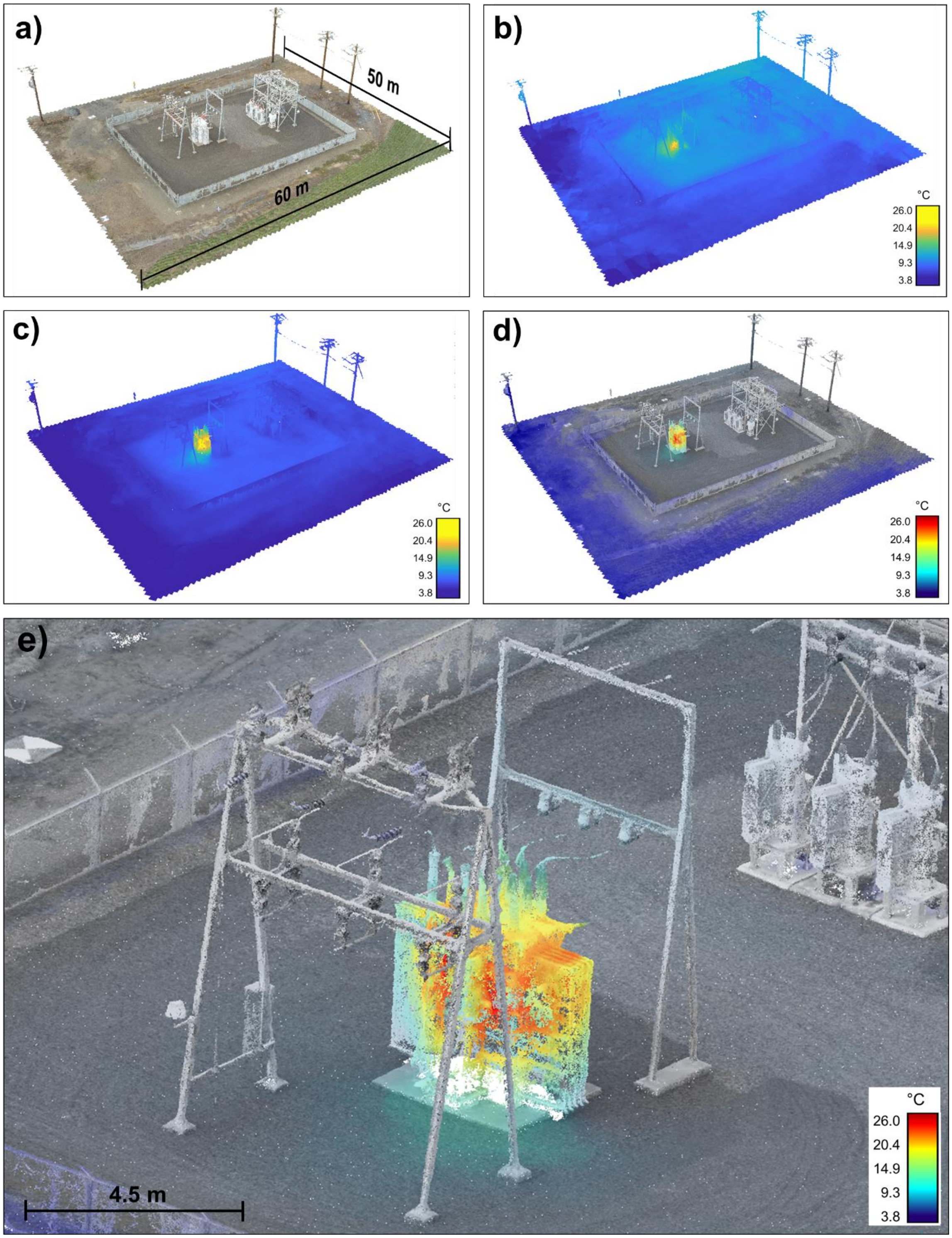


**Figure 10: (a) dense RGB point cloud resulted from Sf M-MVS for Brownsville Power Station (Site 2), (b) TIR 3D point clouds from 3D boresighting approach, (c) TIR 3D point cloud, resulted from 2D image registration approach, (d) fused RGB-TIR 3D point clouds for visualization, and (e) close-up view of fused visualization**

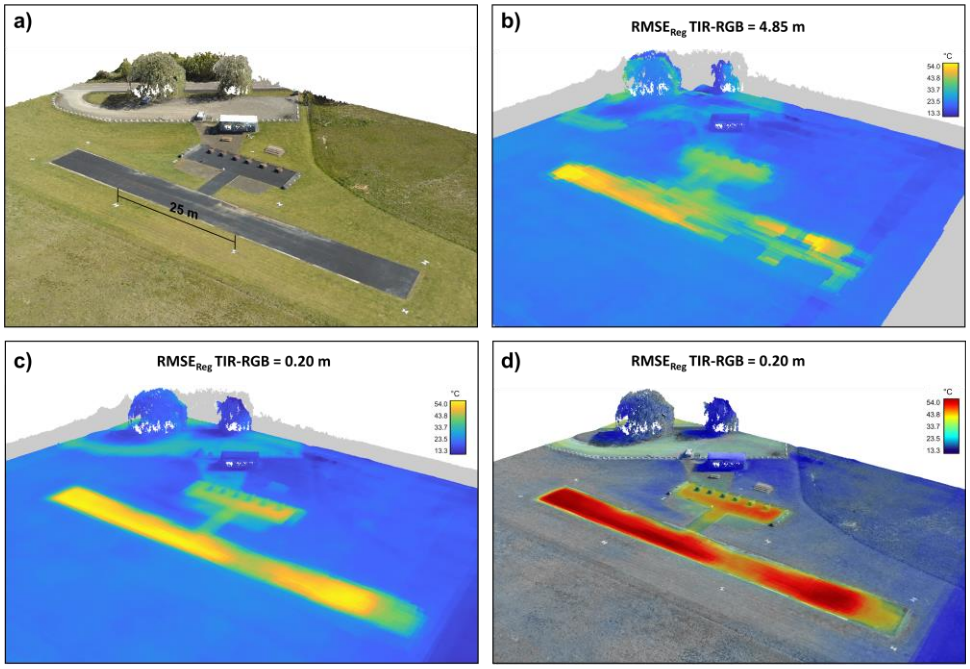


**Figure 11: (a) Dense RGB point cloud resulted from SfM for Adair RC Club (Site 3), (b) TIR 3D point clouds from 3D boresighting approach, (c) TIR 3D point cloud from 2D image registration approach, and (d) fused RGB-TIR 3D point cloud visualization**

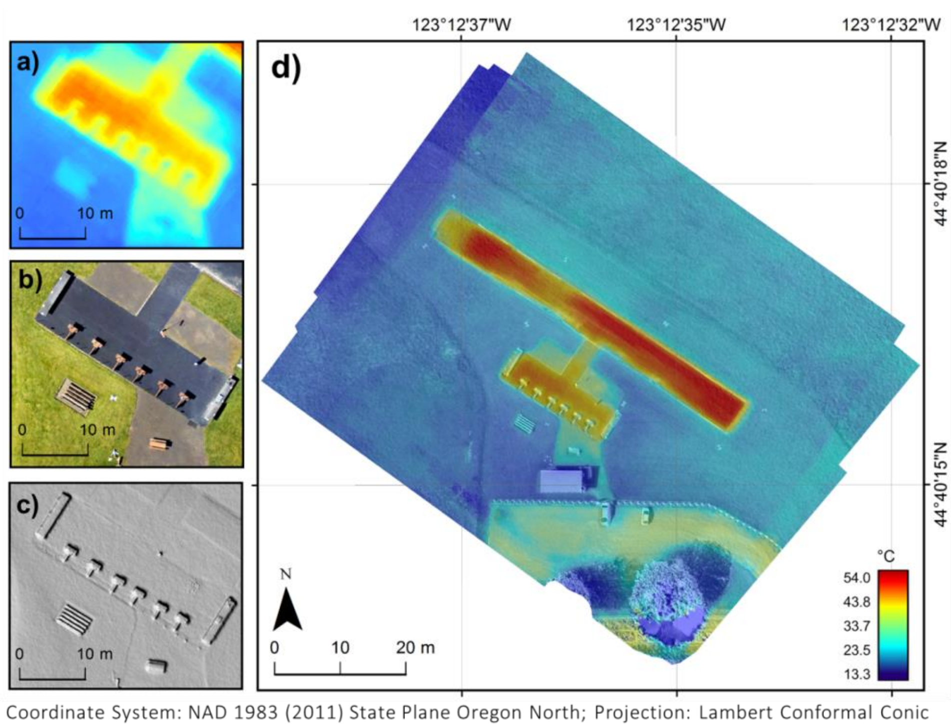


**Figure 12: (a) Color-mapped TIR orthoimage, (b) RGB orthoimage, (c) DEM-based hillshade raster, and (d) the integrated raster made of grayscale of RGB orthoimage fused with hillshade raster, overlaid with 20-percent transparent, color-mapped TIR orthoimage for Site 3.**

## 6. Conclusions and recommendations

Fused TIR and RGB 3D models generated from UAS imagery offer great potential for mapping heat loss, supplementing non-destructive testing of structures, aiding in the inspection of electrical parts, and more. This study tested a simplified approach for generating 3D TIR point clouds from coacquired TIR and RGB images for remote sensing applications. The constructed TIR point clouds are georeferenced to the same coordinate system as the RGB clouds. The resultant point cloud preserves the spatial density and resolution of the RGB point cloud while adding TIR attributes. The integrated visualization approach tested in this study enables 3D point cloud and 2D raster representation of RGB and TIR data in one model, enhancing the visual interpretation and analysis of the remotely-sensed data. The approach does not require additional depth sensors, such as lidar, or GNSS-aided INS for registration purposes.

The average of the intensity readings at thermal images are converted to an absolute temperature value and mapped as additional spectral information of the spatial point. The relative differences between cameras are determined by finding either a 3D boresight rotation and lever-arm between cameras or by finding 2D coordinate transformation parameters to register the TIR and RGB images together. The 3D approach requires accurate multi-camera calibration parameters that are challenging to estimate. In a simplified approach, the 2D approach considers the parallax displacement caused by the stereo view of multi-cameras negligible. Between the 3D and 2D approaches, the former is the more theoretically correct, because it is based on mathematics that model the actual imaging geometry, whereas the latter is akin to a simple image warp. However, comparison of the RMSE of TIR-RGB registration (Figure 9 and Figure 11) shows that the 2D image registration approach performed better, likely as a consequence of the reliance of the 3D approach on accurate geometric camera calibration, which is difficult to achieve for consumer-grade thermal cameras. The 2D approach does not require *a priori* geometric camera calibration and was found to be effective in this study.

In general, the approach is appropriate for cases when processing the overlapping TIR images solely with SfM fails due to lack of features to be matched between photos, or the reconstructed model does not meet accuracy requirements. For evaluation, and as examples of implementation, coacquired TIR and RGB images were collected at three sites using from either a UAS or a handheld device. First, the direct SfM-MVS was used to processes RGB and TIR images separately. While the SfM processing of RGB images was able to generate reliable, RGB dense point clouds, the conventional method on TIR data failed for two of the three sites, and the resultant point cloud for the remaining site was geometrically poor. While a limitation of the approach is that it can only be applied to thermal imagery collected during the day (due to the need for coacquired RGB imagery), it was found in this study to be a reliable, computationally efficient method of producing dense, accurate RGB-TIR point clouds.

In future work, the proposed integration and visualization can be integrated into standard SfM software packages and workflows. Additionally, thermal drift can be corrected by normalization of the images before processing or through post-processing steps by considering the locations pixels. Yet another challenge that can be addressed in future work relates to collecting data over large spatial extents, as temperature changes during the UAS data acquisition can hinder the subsequent merging and analysis of the data products. Radiometric calibration was considered beyond the scope of the present study; however, in-situ radiometric calibration of the thermal camera might improve the spectral content of the data. As an alternative for checkerboard setups in future works, 3D targets can be used to estimate calibration parameters that may improve camera calibration estimations. Time synchronization of multi-camera setups is another major challenge that can significantly impact the mapping quality. TIR-RGB image feature matching and auto-registration can handle non-synchronized dual-head camera captures; however, extraction of identical features and co-registration based on the extracted pair is challenging for images of different spectral bands at the scene without well-designed calibration patterns. It is recommended that follow-on studies be conducted to address these topics.

## Acknowledgments

The funding for this research was provided internally by the School of Civil and Construction Engineering (CCE) at Oregon State University (OSU). The UAS flights were conducted under Federal Aviation Administration (FAA) certificate of authorization (COA) number 2016-WSA-101-COA. We thank Dr. Michael Olsen, Dr. Jihye Park, and Dr. Michael Wing for their valuable comments and suggestions on improving the quality of this paper. We are thankful to Chase Simpson, Greyson Termini, William Gage Maurer, Laura Barreiro Fernández, Dr. Eduardo González-Ferreiro, and Erzhuo Che for their help with collecting the data, and Joseph Fradella for providing the FLIR E6 camera. We would like to acknowledge VDOS Global, OSU Research Office, Pacific Power, Adair RC Club, and Bonneville Power Administration (BPA) and Dr. Roberto Albertani for supplying the logistics for the UAS flight operations. We also appreciate Leica Geosystems, David Evans and Associates, and MicroSurvey for providing surveying equipment and/or software. We would like to thank two anonymous reviewers for their constructive suggestions and comments.

## References

Aasen, Helge, Andreas Burkart, Andreas Bolten, and Georg Bareth. 2015. "Generating 3D Hyperspectral Information with Lightweight UAV Snapshot Cameras for Vegetation Monitoring: From Camera

Calibration to Quality Assurance." *ISPRS Journal of Photogrammetry and Remote Sensing* 108. International Society for Photogrammetry and Remote Sensing, Inc. (ISPRS): 245–259. doi:10.1016/j.isprsjprs.2015.08.002.

Agisoft. 2017. "PhotoScan Professional v1.3." St. Petersburg, Russia: Agisoft LLC.

Allahyari, Mahsa, Michael J. Olsen, Daniel T. Gillins, and Michael L. Dennis. 2018. "Tale of Two RTNs: Rigorous Evaluation of Real-Time Network GNSS Observations." *Journal of Surveying Engineering* 144 (2): 05018001. doi:10.1061/(ASCE)SU.1943-5428.0000249.

Berni, J., P.J. Zarco-Tejada, L. Suarez, and E. Fereres. 2009. "Thermal and Narrowband Multispectral Remote Sensing for Vegetation Monitoring From an Unmanned Aerial Vehicle." *Geoscience and Remote Sensing, IEEE Transactions On* 47 (3): 722–738. doi:10.1109/TGRS.2008.2010457.

Bo Li, Lionel Heng, Kevin Koser, and Marc Pollefeys. 2013. "A Multiple-Camera System Calibration Toolbox Using a Feature Descriptor-Based Calibration Pattern." In *2013 IEEE/RSJ International Conference on Intelligent Robots and Systems*, 1301–1307. IEEE. doi:10.1109/IROS.2013.6696517.

Borrmann, Dorit, Andreas Nüchter, Marija Đakulović, Ivan Maurović, Ivan Petrović, Dinko Osmanković, and Jasmin Velagić. 2014. "A Mobile Robot Based System for Fully Automated Thermal 3D Mapping." *Advanced Engineering Informatics* 28 (4): 425–440. doi:10.1016/j.aei.2014.06.002.

Bouguet, Jean-Yves. 2004. "Camera Calibration Toolbox for MATLAB."

Brook, Anna, Marijke Vandewal, and Eyal Ben-Dor. 2012. "Fusion of Optical and Thermal Imagery and LiDAR Data for Application to 3-D Urban Environment and Structure Monitoring." In *Remote Sensing - Advanced Techniques and Platforms*. InTech. doi:10.5772/36066.

Choi, Kyuha, Changhyun Kim, and Jong Beom Ra. 2010. "Infrared Image Enhancement Based on an Aligned High Resolution Visible Image." In *2010 IEEE International Conference on Image Processing*, 3341–3344. IEEE. doi:10.1109/ICIP.2010.5651482.

Colomina, I., and P. Molina. 2014. "Unmanned Aerial Systems for Photogrammetry and Remote Sensing: A Review." *ISPRS Journal of Photogrammetry and Remote Sensing* 92 (June): 79–97. doi:10.1016/j.isprsjprs.2014.02.013.

Dios, J. R. Martinez-De, and A. Ollero. 2006. "Automatic Detection of Windows Thermal Heat Losses in Buildings Using UAVs." In *2006 World Automation Congress*, 1–6. IEEE. doi:10.1109/WAC.2006.375998.

Ellmauthaler, Andreas, Eduardo A. B. da Silva, Carla L. Pagliari, Jonathan N. Gois, and Sergio R. Neves. 2013. "A Novel Iterative Calibration Approach for Thermal Infrared Cameras." In *2013 IEEE International Conference on Image Processing*, 2182–2186. IEEE. doi:10.1109/ICIP.2013.6738450.

Eltner, Anette, Andreas Kaiser, Carlos Castillo, Gilles Rock, Fabian Neugirg, and Antonio Abellán. 2016. "Image-Based Surface Reconstruction in Geomorphometry – Merits, Limits and Developments." *Earth Surface Dynamics* 4 (2): 359–389. doi:10.5194/esurf-4-359-2016.

Esri. 2016. "ArcGIS Desktop V10.2.2." Redlands, CA: Esri. http://desktop.arcgis.com/en/.

FLIR. 2018. "Ex-Series™." Accessed February 9. http://www.flir.com/instruments/ex-series/.

Furukawa, Yasutaka, and Jean Ponce. 2010. "Accurate, Dense, and Robust Multiview Stereopsis." *IEEE Transactions on Pattern Analysis and Machine Intelligence* 32 (8). IEEE: 1362–1376. doi:10.1109/TPAMI.2009.161.

Gade, Rikke, and Thomas B. Moeslund. 2014. "Thermal Cameras and Applications: A Survey." *Machine Vision and Applications* 25 (1): 245–262. doi:10.1007/s00138-013-0570-5.

Ghilani, Charles D. 2011. *Adjustment Computations: Spatial Data Analysis*. John Wiley & Sons.

Girardeau-Montaut, D. 2017. "Cloud Compare: 3D Point Cloud and Mesh Processing Software, Open-

Source Project.” *Open Source Project*. http://www.danielgm.net/cc/.

González-Aguilera, D., P. Rodriguez-Gonzalvez, J. Armesto, and S. Lagüela. 2012. “Novel Approach to 3D Thermography and Energy Efficiency Evaluation.” *Energy and Buildings* 54 (November): 436–443. doi:10.1016/j.enbuild.2012.07.023.

Guo, Qinghua, Wenkai Li, Hong Yu, and Otto Alvarez. 2010. “Effects of Topographic Variability and Lidar Sampling Density on Several DEM Interpolation Methods.” *Photogrammetric Engineering & Remote Sensing* 76 (6): 701–712. doi:10.14358/PERS.76.6.701.

Ham, Youngjib, and Mani Golparvar-Fard. 2013. “An Automated Vision-Based Method for Rapid 3D Energy Performance Modeling of Existing Buildings Using Thermal and Digital Imagery.” *Advanced Engineering Informatics* 27 (3). Elsevier Ltd: 395–409. doi:10.1016/j.aei.2013.03.005.

Harris, Chris, and Mike Stephens. 1988. “A COMBINED CORNER AND EDGE DETECTOR.” *Alvey Vision Conference* 15: 50.

Harris Geospatial. 2014. “ENVI v5.2.” Melbourne, FL: Harris Corporation. http://www.harrisgeospatial.com/ProductsandTechnology/Software/ENVI.aspx.

Heikkila, Janne, and Olli Silven. 1997. “A Four-Step Camera Calibration Procedure with Implicit Image Correction.” In *Computer Vision and Pattern Recognition, 1997. Proceedings., 1997 IEEE Computer Society Conference On*, 1106–1112.

Hoegner, L., T. Abmayr, D. Tosic, S. Turzer, and U. Stilla. 2018. “FUSION OF 3D POINT CLOUDS WITH TIR IMAGES FOR INDOOR SCENE RECONSTRUCTION.” *ISPRS - International Archives of the Photogrammetry, Remote Sensing and Spatial Information Sciences* XLII-1 (October): 189–194. doi:10.5194/isprs-archives-XLII-1-189-2018.

Hoegner, L, S. Tuttas, Y. Xu, K. Eder, and U. Stilla. 2016. “EVALUATION OF METHODS FOR COREGISTRATION AND FUSION OF RPAS-BASED 3D POINT CLOUDS AND THERMAL INFRARED IMAGES.” *ISPRS - International Archives of the Photogrammetry, Remote Sensing and Spatial Information Sciences* XLI-B3 (June). IEEE: 241–246. doi:10.5194/isprs-archives-XLI-B3-241-2016.

Honkavaara, Eija, Tomi Rosnell, Raquel Oliveira, and Antonio Tommaselli. 2017. “Band Registration of Tuneable Frame Format Hyperspectral UAV Imagers in Complex Scenes.” *ISPRS Journal of Photogrammetry and Remote Sensing* 134. The Authors: 96–109. doi:10.1016/j.isprsjprs.2017.10.014.

Iyengar, S.S., S. Sastry, and N. Balakrishnan. 2003. “Foundations of Data Fusion for Automation.” *IEEE Instrumentation & Measurement Magazine* 6 (4): 35–41. doi:10.1109/MIM.2003.1251481.

Javadnejad, Farid. 2013. “Flood Inundation Mapping Using HEC-RAS and GIS for Shelby County, Tennessee.” University of Memphis.

Javadnejad, Farid. 2018. “Small Unmanned Aircraft Systems (UAS) for Engineering Inspections and Geospatial Mapping.” Oregon State University. http://ir.library.oregonstate.edu/concern/graduate_thesis_or_dissertations/6969z572s.

Javadnejad, Farid, Firooz Alinia, and Pouran Behnia. 2011. “Targeting Structural Features and Alterations for Reconnaissance of Hydrothermal Gold Mineralization in Delijan Area Using DEM and ETM+ Data.” *Amirkabir Journal of Science and Technology* 72 (21): 9–16.

Javadnejad, Farid, and Daniel T. Gillins. 2016. “Unmanned Aircraft Systems-Based Photogrammetry for Ground Movement Monitoring.” In *Pipelines 2016*, 1000–1011. Reston, VA: American Society of Civil Engineers. doi:10.1061/9780784479957.094.

Javadnejad, Farid, Daniel T. Gillins, Christopher C. Higgins, and Matthew N. Gillins. 2017. “BridgeDex : Proposed Web GIS Platform for Managing and Interrogating Multiyear and Multiscale Bridge-

Inspection Images." *Journal of Computing in Civil Engineering* 31 (6): 04017061. doi:10.1061/(ASCE)CP.1943-5487.0000710.

Javadnejad, Farid, Matthew N. Gillins, and Daniel T. Gillins. 2016. "Vertical Accuracy Assessment of Image-Based Reconstructed 3D Point Clouds with Respect to Horizontal Ground Sampling Distance." In *ASPRS Annual Conference, Imaging & Geospatial Technology Forum (IGTF) 2016*. Fort Worth, TX: ASPRS.

Javadnejad, Farid, Chase H. Simpson, Daniel T. Gillins, Tyler Claxton, and Michael J. Olsen. 2017. "An Assessment of UAS-Based Photogrammetry for Civil Integrated Management (CIM) Modeling of Pipes." In *Pipelines 2017*, 112–123. Reston, VA: American Society of Civil Engineers. doi:10.1061/9780784480885.012.

Javadnejad, Farid, Brian Waldron, and Arleen Hill. 2017. "LITE Flood: Simple GIS-Based Mapping Approach for Real-Time Redelineation of Multifrequency Floods." *Natural Hazards Review* 18 (3): 04017004. doi:10.1061/(ASCE)NH.1527-6996.0000238.

Jensen, John R. 2009. *Remote Sensing of the Environment: An Earth Resource Perspective*. 2nd ed. New Delhi, India: Pearson Education India.

Kylili, Angeliki, Paris A. Fokaides, Petros Christou, and Soteris A. Kalogirou. 2014. "Infrared Thermography (IRT) Applications for Building Diagnostics: A Review." *Applied Energy* 134: 531–549. doi:10.1016/j.apenergy.2014.08.005.

Lague, Dimitri, Nicolas Brodu, and Jérôme Leroux. 2013. "Accurate 3D Comparison of Complex Topography with Terrestrial Laser Scanner: Application to the Rangitikei Canyon (N-Z)." *ISPRS Journal of Photogrammetry and Remote Sensing* 82 (August): 10–26. doi:10.1016/j.isprsjprs.2013.04.009.

Lagüela, S., L. Díaz-Vilariño, and D. Roca. 2016. "Infrared Thermography: Fundamentals and Applications." In , edited by B. Riveiro and M. Solla, 113–138. CRC Press. doi:10.1201/b19024-8.

Le Moigne, J., W.J. Campbell, and R.F. Cromp. 2002. "An Automated Parallel Image Registration Technique Based on the Correlation of Wavelet Features." *IEEE Transactions on Geoscience and Remote Sensing* 40 (8). IEEE: 1849–1864. doi:10.1109/TGRS.2002.802501.

Lewis, A., G.E. Hilley, and J.L. Lewicki. 2015. "Integrated Thermal Infrared Imaging and Structure-from-Motion Photogrammetry to Map Apparent Temperature and Radiant Hydrothermal Heat Flux at Mammoth Mountain, CA, USA." *Journal of Volcanology and Geothermal Research* 303 (September). Elsevier B.V.: 16–24. doi:10.1016/j.jvolgeores.2015.07.025.

Lowe, David G. 2004. "Distinctive Image Features from Scale-Invariant Keypoints." *International Journal of Computer Vision* 60 (2): 91–110. doi:10.1023/B:VISI.0000029664.99615.94.

Lucieer, Arko, Zbyněk Malenovský, Tony Veness, and Luke Wallace. 2014. "HyperUAS-Imaging Spectroscopy from a Multirotor Unmanned Aircraft System." *Journal of Field Robotics* 31 (4): 571–590. doi:10.1002/rob.21508.

Mahmoudabadi, Hamid, Michael J. Olsen, and Sinisa Todorovic. 2016. "Efficient Terrestrial Laser Scan Segmentation Exploiting Data Structure." *ISPRS Journal of Photogrammetry and Remote Sensing* 119 (September). International Society for Photogrammetry and Remote Sensing, Inc. (ISPRS): 135–150. doi:10.1016/j.isprsjprs.2016.05.015.

Maset, E., A. Fusiello, F. Crosilla, R. Toldo, and D. Zorzetto. 2017. "PHOTOGRAMMETRIC 3D BUILDING RECONSTRUCTION from THERMAL IMAGES." *ISPRS Annals of the Photogrammetry, Remote Sensing and Spatial Information Sciences* 4 (2W3): 25–32. doi:10.5194/isprs-annals-IV-2-W3-25-2017.

Mikhail, Edward M, James S Bethel, and J Chris McGlone. 2001. "Introduction to Modern

Photogrammetry." *New York*.

Nagi, R. 2012. "Maintaining Detail and Color Definition When Integrating Color and Grayscale Rasters Using No Alteration of Grayscale or Intensity (NAGI) Fusion Method." In *Proceedings*, 16–18.

Nishar, Abdul, Steve Richards, Dan Breen, John Robertson, and Barbara Breen. 2016. "Thermal Infrared Imaging of Geothermal Environments and by an Unmanned Aerial Vehicle (UAV): A Case Study of the Wairakei – Tauhara Geothermal Field, Taupo, New Zealand." *Renewable Energy* 86 (February): 1256–1264. doi:10.1016/j.renene.2015.09.042.

O'Banion, Matt S., Michael J. Olsen, Claire Rault, Joseph Wartman, and Keith Cunningham. 2018. "Suitability of Structure from Motion for Rock-Slope Assessment." *The Photogrammetric Record* 33 (162): 217–242. doi:10.1111/phor.12241.

Pajares, Gonzalo. 2015. "Overview and Current Status of Remote Sensing Applications Based on Unmanned Aerial Vehicles (UAVs)." *Photogrammetric Engineering & Remote Sensing* 81 (4): 281–330. doi:10.14358/PERS.81.4.281.

Pix4D. 2017. "Pix4Dmapper Pro v4.0." Lausanne, Switzerland: Pix4D. https://pix4d.com/product/pix4dmapper-photogrammetry-software/.

Roth, M., T. R. Oke, and W. J. Emery. 1989. "Satellite-Derived Urban Heat Islands from Three Coastal Cities and the Utilization of Such Data in Urban Climatology." *International Journal of Remote Sensing* 10 (11): 1699–1720. doi:10.1080/01431168908904002.

Roy, DP, MA Wulder, TR Loveland, Woodcock C.E., R.G. Allen, M.C. Anderson, D. Helder, et al. 2014. "Landsat-8: Science and Product Vision for Terrestrial Global Change Research." *Remote Sensing of Environment* 145 (April): 154–172. doi:10.1016/j.rse.2014.02.001.

Salvi, Joaquim, Xavier Armangué, and Joan Batlle. 2002. "A Comparative Review of Camera Calibrating Methods with Accuracy Evaluation." *Pattern Recognition* 35 (7): 1617–1635. doi:10.1016/S0031-3203(01)00126-1.

senseFly. 2017. "SenseFly® Albris." https://www.sensefly.com/drones/albris.html.

Shao, Zhenfeng, Nan Yang, Xiongwu Xiao, Lei Zhang, and Zhe Peng. 2016. "A Multi-View Dense Point Cloud Generation Algorithm Based on Low-Altitude Remote Sensing Images." *Remote Sensing* 8 (5): 381. doi:10.3390/rs8050381.

Shi, Yeyin, J. Alex Thomasson, Seth C. Murray, N. Ace Pugh, William L. Rooney, Sanaz Shafian, Nithya Rajan, et al. 2016. "Unmanned Aerial Vehicles for High-Throughput Phenotyping and Agronomic Research." Edited by Jinfa Zhang. *PLOS ONE* 11 (7): e0159781. doi:10.1371/journal.pone.0159781.

Singh, Kunwar K., and Amy E. Frazier. 2018. "A Meta-Analysis and Review of Unmanned Aircraft System (UAS) Imagery for Terrestrial Applications." *International Journal of Remote Sensing*, January, 1–21. doi:10.1080/01431161.2017.1420941.

Sledz, A, J Unger, and C Heipke. 2018. "THERMAL IR IMAGING: IMAGE QUALITY AND ORTHOPHOTO GENERATION." In *ISPRS - International Archives of the Photogrammetry, Remote Sensing and Spatial Information Sciences*, XLII-1:413–420. doi:10.5194/isprs-archives-XLII-1-413-2018.

Slocum, Richard K., and Christopher E. Parrish. 2017. "Simulated Imagery Rendering Workflow for UAS-Based Photogrammetric 3D Reconstruction Accuracy Assessments." *Remote Sensing* 9 (4): 396. doi:10.3390/rs9040396.

Snavely, Noah, Steven M. Seitz, and Richard Szeliski. 2006. "Photo Tourism." In *ACM SIGGRAPH 2006 Papers on - SIGGRAPH '06*, 25:835. New York, New York, USA: ACM Press. doi:10.1145/1179352.1141964.

Snavely, Noah, Steven M. Seitz, and Richard Szeliski. 2008. "Modeling the World from Internet Photo Collections." *International Journal of Computer Vision* 80 (2): 189–210. doi:10.1007/s11263-007-0107-3.

Szeliski, Richard. 2010. *Computer Vision: Algorithms and Applications*. 1st ed. New York, NY, USA: Springer-Verlag New York, Inc.

Tahami, Hoda, Anahid Basiri, Terry Moore, Jihye Park, and Lukasz Bonenberg. 2018. "Virtual Spatial Diversity Antenna for GNSS Based Mobile Positioning in the Harsh Environments." In , 3186–3198. doi:10.33012/2018.15987.

Teillet, P.M, J.L Barker, B.L Markham, R.R Irish, G. Fedosejevs, and J.C Storey. 2001. "Radiometric Cross-Calibration of the Landsat-7 ETM+ and Landsat-5 TM Sensors Based on Tandem Data Sets." *Remote Sensing of Environment* 78 (1–2): 39–54. doi:10.1016/S0034-4257(01)00248-6.

Tommaselli, Antonio, M. Galoa, J. Marcato Junior, R. S. Ruy, and R. F. Lopes. 2010. "Registration and Fusion of Multiple Images Acquired With Medium Format Cameras." In *The 2010 Canadian Geomatics Conference and Symposium of Commission I - ISPRS Convergence in Geomatics*. Calgary, Alberta, Canada. doi:10.13140/2.1.3064.0329.

Triggs, Bill, Philip F McLauchlan, Richard I Hartley, and Andrew W Fitzgibbon. 1999. "Bundle Adjustment—a Modern Synthesis." In *International Workshop on Vision Algorithms*, 298–372.

Vidas, Stephen, Peyman Moghadam, and Michael Bosse. 2013. "3D Thermal Mapping of Building Interiors Using an RGB-D and Thermal Camera." *Proceedings - IEEE International Conference on Robotics and Automation*, 2311–2318. doi:10.1109/ICRA.2013.6630890.

Vidas, Stephen, Peyman Moghadam, and Sridha Sridharan. 2015. "Real-Time Mobile 3D Temperature Mapping." *IEEE Sensors Journal* 15 (2): 1145–1152. doi:10.1109/JSEN.2014.2360709.

Wood, R.L., Daniel T. Gillins, M.E. Mohammadi, Farid Javadnejad, H. Tahami, Matthew N. Gillins, and Y. Liao. 2017. "2015 Gorkha Post-Earthquake Reconnaissance of a Historic Village with Micro Unmanned Aerial Systems." In *16th World Conference on Earthquake (16WCEE)*. International Association for Earthquake Engineering (IAEE).

Wu, Changchang. 2011. "VisualSFM: A Visual Structure from Motion System."

Yilmaz, Alper, Khurram Shafique, and Mubarak Shah. 2003. "Target Tracking in Airborne Forward Looking Infrared Imagery." *Image and Vision Computing* 21 (7): 623–635. doi:10.1016/S0262-8856(03)00059-3.

Zhang, Jixian. 2010. "Multi-Source Remote Sensing Data Fusion: Status and Trends." *International Journal of Image and Data Fusion* 1 (1): 5–24. doi:10.1080/19479830903561035.